Metallography, Microstructure, and Analysis (2020) 9:744–758
https://doi.org/10.1007/s13632-020-00688-5

TECHNICAL ARTICLE

Microstructural Characteristics of the Al Alloys: The Dissimilarities Among the 2XXX Alloys Series used in Aircraft Structures

João Victor de Sousa Araujo[1] · **Mariana Xavier Milagre**[1] · **Raphael Oliveira Ferreira**[2] · **Caruline de Souza Carvalho Machado**[1] · **Caio Palumbo de Abreu**[1] · **Isolda Costa**[1]

Received: 4 August 2020 / Revised: 21 September 2020 / Accepted: 29 September 2020 / Published online: 15 October 2020

Abstract

Microstructure characteristics of two high-strength aluminum alloys, the 2024-T3 Al–Cu–Mg, and the new generation Al–Cu–Li alloy 2198, in the T8 and T851 tempers, were investigated in this study. For this purpose, microstructural and statistical analyses were carried out. The results showed equiaxed grains for the 2024-T3 and 2198-T851 alloys, whereas, elongated grains for the 2198-T8. Besides, the 2198-T851 alloy displayed slip bands in the grains due to the stretching stage, "51". The 2024-T3 alloy showed at least two types of constituent particles, Al–Cu–Mg and Al–Cu–Mn–Fe–(Si); whereas Al–Cu–Li alloys showed only one type, Al–Cu–Fe, in their composition. Statistical analyses showed that the percentage of area covered by constituent particles was larger in the 2024-T3 alloy compared to the 2198 in both tempers, T8 and T851. On the other hand, the Al–Cu–Li alloys showed higher microhardness values relatively to the Al–Cu one. The differences among the nanometric phases present in Al–Cu and Al–Cu–Li alloys were analyzed by transmission electron microscopy. All the results were related to the different chemical composition and industrial thermomechanical processing of each alloy.

Keywords Al–Cu–Mg alloy · Al–Cu–Li alloy · Microstructure · Statistical analysis · SEM · TEM

Introduction

In the last decades, the aerospace industry has been innovative in the development of lighter materials with improved mechanical resistance [1, 2]. Al alloys have been widely used by aeronautic industries mainly in commercial aircraft [3, 4]. The aircraft structure is usually composed of about 70% of Al alloys, 7% of Ti alloys, 11% of steel plates, 11% of composites, and 1% of other materials [5]. The Al alloys belonging to 2XXX series are the most used materials in the aircraft manufacturing [3–6]. They are applied as fuselage/pressure cabin, upper wing, lower wing, horizontal stabilizers, being constantly submitted to various types of service loading. Thus, properties such as elastic modulus, compressive yield strength, tensile strength, fatigue, fatigue crack growth, fracture toughness and corrosion resistance are required [7].

The 2024 alloy stands out in aircraft applications [8, 9]. Nevertheless, the search for lighter materials resulted in the development of the Al–Cu–Li alloys [10, 11]. The addition of Li in the Al–Cu alloys has been reported to reduce their density and increase their elastic modulus [12]. These alloys show excellent properties for aeronautic applications, and could replace the 2024 alloy [13]. For instance, compared to the conventional Al alloys, the Al–Cu–Li one promotes a weight reduction that varies from 7 to 14%, according to the component replaced (fuselage, upper wing and skin) [5]. Among the Al–Cu–Li alloys, the 2198 one has been attracting much attention. It has 0.8–1.1 wt% of Li in its composition [8, 10, 14, 15]. Currently, this alloy has been applied in the structures of the C919 commercial aircraft manufactured by Commercial Aircraft Corporation of China Ltd. (COMAC) [16–18], which competes with Airbus A320 and Boeing 737 in the aircraft market.

Many researchers have investigated the dissimilarities between Al–Cu and Al–Cu–Li alloys, such as: the influence of industrial thermomechanical process in the alloys'

✉ João Victor de Sousa Araujo
joao-neutron@hotmail.com

[1] Materials Science and Technology Center, Nuclear and Energy Research Institute—IPEN/CNEN , Av. Prof. Lineu Prestes, São Paulo 2242, Brazil

[2] Surface Phenomena Laboratory, Polytechnic School of the University of São Paulo, Av. Prof. Mello Moraes, São Paulo 2463, Brazil

mechanical properties [19, 20], exfoliation/intragranular corrosion resistance [21–24] and the differences between the electrochemical behavior of these alloys [25–27]. In the literature, some properties of the 2024 and 2198 alloys, specifically fatigue [28–35] and corrosion resistance [36–40] were investigated and compared.

The microstructure of the materials influences their physical and chemical properties, such as hardness [41], roughness [42, 43], elasticity [44–46], plasticity [45, 47], anodizing ability [48–53], electrochemical behavior [54–56], corrosion resistance [57–59]. Therefore, it is very important to investigate the microstructure characteristics of the materials.

The Al-alloys microstructure is composed by coarse intermetallic particles (size range of 1–50 µm), dispersoids (varying from 0.05 to 0.5 µm), and fine precipitates (with sizes 1–100 nm) [60]. The microstructure characteristics of conventional Al–Cu alloys and the third-generation of Al–Cu–Li alloys are mainly influenced by their chemical composition. The composition variation between these alloys is responsible for the different nature of their micrometric and nanometric particles, and this justifies a detailed investigation of these characteristics. However, this matter has not yet received the deserved attention and is scarcely reported in the literature.

In order to assure the good performance of aircraft components the study of the microstructure of the alloys employed in their fabrication is of fundamental importance. Differences related to the expected microstructure and that obtained after material processing have a great impact on the component corrosion resistance and its mechanical properties. Moreover, concerns on the climate changes require efforts from the materials researchers to develop materials that lead to reduction in gas emissions volume. In this way, this paper investigates the microstructure of the conventional 2024-T3 alloy and the new generation 2198 Al–Cu–Li alloy in the tempers T8 and T851, showing the differences and similarities between these two types of alloys.

Materials

The chemical composition of the alloys used in this study is presented in Table 1. The alloys were evaluated maintaining their original commercial tempers, specifically T3 (2024), T8 (2198), and T851 (2198). The description of these tempers [61] is shown in Table 2.

Surface Preparation

The surface of the studied samples was ground with silicon carbide paper up to #4000 and, then, polished with diamond suspensions of 3 µm and 1 µm. The surface of the alloys was observed after etching in a solution with 2 (v/v)% hydrofluoric and 25 (v/v)% nitric acid.

Table 1. Chemical composition of the alloys (wt%) obtained by inductively coupled plasma optical emission spectrometry (ICP-OES)

Elements	Aluminum alloys		
	2024-T3	2198-T8	2198-T851
Al	Balance	Balance	Balance
Cu	4.8	3.34	3.31
Mg	0.59	0.31	0.31
Mn	0.52	0.003	0.003
Li	–	0.95	0.96
Fe	0.18	0.04	0.04
Zn	0.11	0.006	0.006
Si	0.07	0.04	0.03
Zr	–	0.50	0.40
Ag	–	0.26	0.25

Microhardness Measurements

Microhardness measurements were carried out in a Buehler 1600 series Microhardness equipment using a load of 300 g for a dwell time of 15 s. A total of 40 measurements were recorded for each alloy and, then, the mean values were estimated.

Optical Microscopy (OM)

The microstructure of each alloy was observed by optical microscope using a Leica DMLM equipment coupled to a Leica EC3 camera and controlled by a LAS ES software.

Scanning Electron Microscopy (SEM)

Analysis of the alloys microstructure of was also carried out by SEM using a JSM-6701F microscope equipped with energy dispersive X-ray spectroscopy (EDS) detectors.

Transmission Electron Microscopy (TEM)

The nanometric phases were analyzed by transmission electron microscopy (TEM) by means of a JEM-2100 microscope, operating at 200 kV. The analyzed samples were prepared by grounding with SiC paper #1200 until reaching an average thickness of 100 µm. Then, discs of approximately 2 mm of diameter were prepared. Subsequently, the discs were grounded until an appropriate thickness for electrolytic etching was reached. Electrolytic etching was performed using a TenuPol equipment and a stainless steel plate as cathode. The electrolyte used was composed of a mixture of

Table 2. Tempers condition for the aluminum alloys used in this study and information relevant to the process

Designation of temper	Description	Aging time (h)	Aging temperature (°C)
T3	Solution heat treated, cold worked, and naturally aged	10–20	160–250
T8	Solution heat treated, cold worked, and artificially aged		
T851	Solution heat treated, stretching with a permanent set from 1.5 to 3%, and then artificially aged		

20% nitric acid in methanol. The voltage during etching was maintained at 25 V and the temperature at – 30 °C. Selected area electron diffraction (SAED) patterns were recorded with a Gatan ES500W camera.

Image Analyzer to Microstructural Characterization

Statistical analysis of each alloy was performed using ImageJ® software. Grain size was estimated from a set of 120 grains and the number of particles per area was assessed by analysis of 40 images for each alloy.

Results and Discussion

The studied alloys presented different grain morphologies, as shown in Figs. 1 and 2. Equiaxed grains were observed for the 2024-T3 and the 2198-T851 alloys, whereas elongated ones for the 2198-T8. Furthermore, the 2198-T851 was the only alloy to show slip bands in preferential grains. As observed in Fig. 1, the grain indicated by letter "A" presents slip bands, whereas that by letter "B" does not show this feature.

Slip bands are favored by the T851 process, since deformation is not uniform during the stretching stage. Consequently, some grains will be more deformed than others, favoring slip bands in those grains. The presence of slip bands in the 2198-T851 alloy is due to the higher percentage of cold work (%CW) that this alloy has been exposed during its processing [62]. Besides, as the stretching stage was performed in two directions, the slip bands are seen in two different orientations. These microstructural features are responsible for the anisotropy of mechanical properties, particularly the yield strength, related to this temper [63]. The elongated grains observed in 2198-T8 reveal a strong textured material with grains preferentially orientated in the deformation direction [63].

The 2198 alloy is applied in different places of the aircraft structure, consequently, different microstructures are required to guarantee the best performance in service of

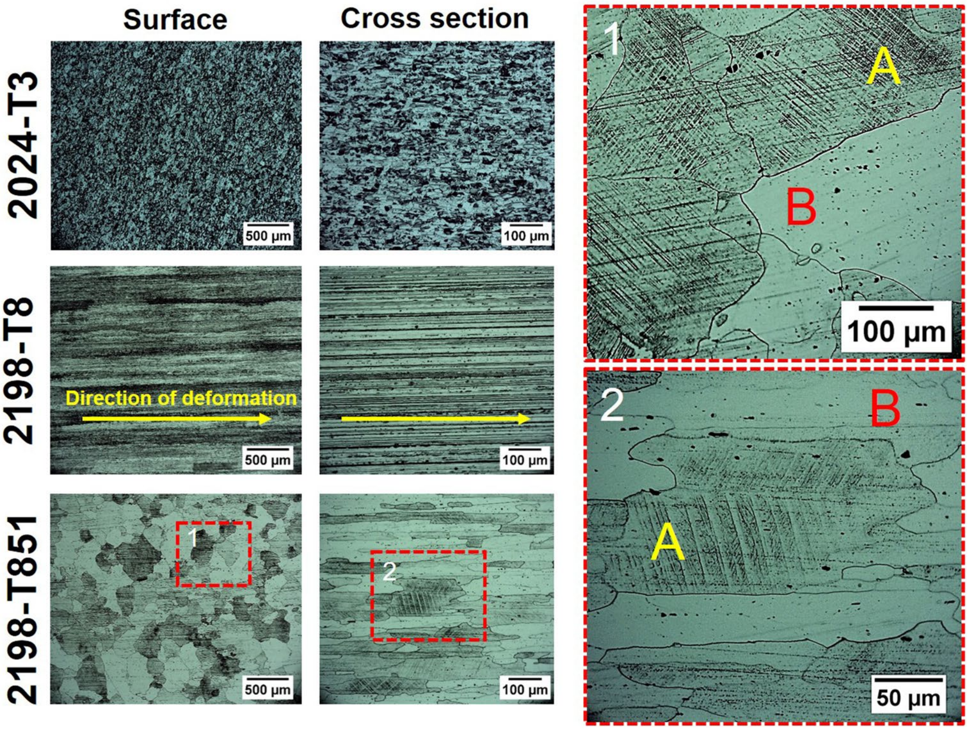

Fig. 1. Optical micrographs of the 2024-T3, 2198-T8, and 2198-T851 alloys. The yellow arrow indicates the deformation direction, and the letters "A" and "B" indicate the grains with and without slip bands, respectively.

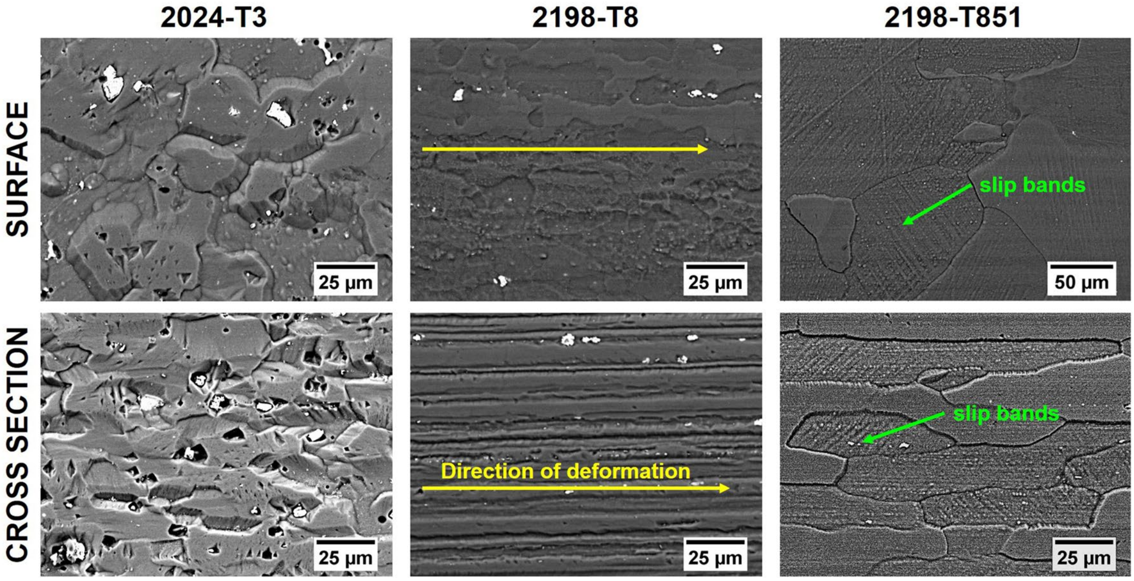

Fig. 2. Scanning electron micrographs of the 2024-T3, 2198-T8, and 2198-T851 alloys after etching. The yellow and green arrows indicate the deformation direction, and the grains with slip bands, respectively.

the components made with this alloy. The grain sizes of the alloys were estimated, as shown in Fig. 3. The corresponding statistical data are presented in Table 3. The grain size of the 2024-T3 alloy is ten times lower than that of the 2198-T851 alloy. Considering the 2198-T8 alloy, due to its strong deformed microstructure, the grain size cannot be directly compared to the other tested alloys; however, the length and width of grains were calculated. The grain width in the 2198-T8 alloy presents an intermediary value between that of the other alloys, and, its grain length greatly exceeded that of the others, especially the 2024-T3 alloy.

Grain size of a material is dependent of its chemical composition, processing and heat treatment. The materials used in this study present different chemical composition, levels of deformation and heat treatment parameters (temperature, time, etc). Therefore, a direct comparison between the alloys grain size is not possible. However, by observation of the alloys microstructure, it is perceptible that the level

Fig. 3. Histogram of the grain size distribution of the 2024-T3, 2198-T8, and 2198-T851 alloys.

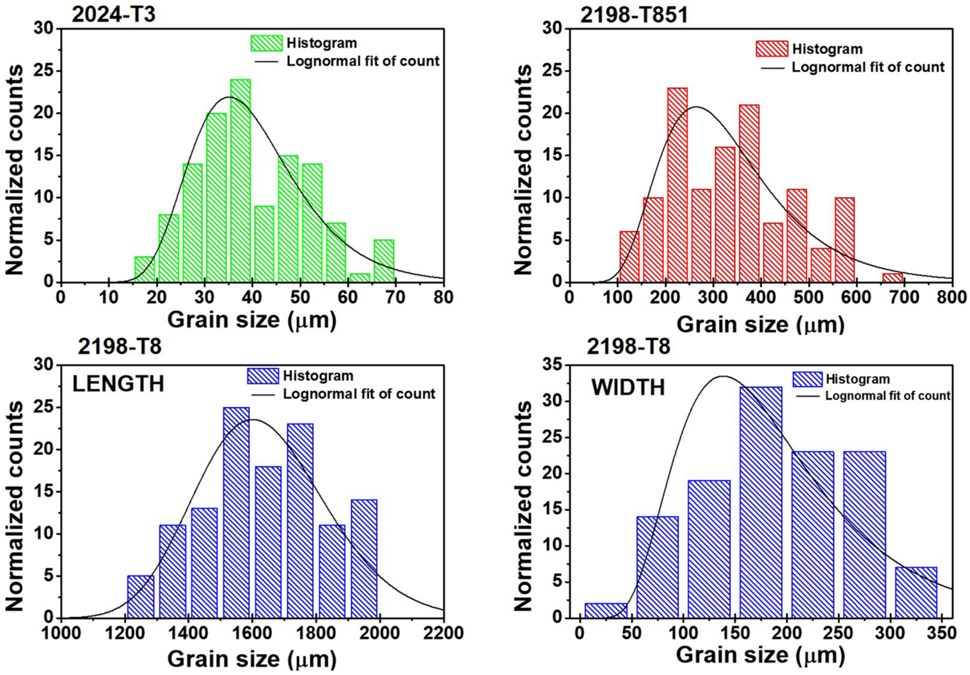

Table 3. Statistical data of grains size of the alloys used in this study

Statistic data	Aluminum alloys			
	2024-T3	2198-T8		2198-T851
		Length	Width	
Mean	40.05	1639.09	188.04	335.41
Standard deviation	11.51	203.88	72.3	128.67
Median	37.71	1624.37	183.52	320.29
Mode	33.83	1561.11	83.52	364.26
Minimum	16.67	1208.97	31.42	667.46
Maximum	67.18	1997.92	338.95	113.14
Count	120	120	120	120

of deformation and treatment temperatures reached for the 2198-T8 and 2198-T851 alloys are not sufficient to promote grains recrystallization for the T8 condition. Despite the fact that both alloys, 2024-T3 and 2198-T851, presented equiaxed grains, the differences in their grain sizes are related to their chemical composition and the degree of cold work to which they were exposed. For instance, the 2198-T851 alloy was exposed to a stretching step followed by artificial aging, whereas the 2024-T3 alloy was naturally aged (at room temperature).

Grain size has an assessable effect on the main mechanical properties of the material, such as: tensile strength, ductility, machinability [64]. For example, decreasing the grain size, results in increase in hardness, yield strength, tensile strength, fatigue strength, and impact strength [65]. Grain size also influences corrosion resistance. According to Ralston et al. [66], decrease in grain size resulted in E_{corr} ennoblement and reduced corrosion susceptibility of pure Al. However, different from pure Al, mechanical and corrosion properties of the Al-alloys are mainly affected by precipitation of second particles during aging processes [67, 68].

Fatigue resistance is also an important concern in the aircraft industry. Yin et al. [69] studied the effect of grain size on fatigue-crack growth in 2524 alloy, which is similar to the 2024 one. Nevertheless, as observed for corrosion resistance, the grain size affects fatigue only when hardening precipitates are absent in the alloy. In this case, as the grain size increased, the fatigue-crack-growth rate decreased significantly.

Alexopoulos et al. [28–30] and Moreto et al. [35], studied the fatigue corrosion resistance of the 2024, 2198, and 2524 alloys and found that second particles in the Al-alloys influences their resistance to fatigue-crack growth due to their different nature in relation to the matrix. Additionally Blanc and Mankowski [70] also reported as the particles sizes influences the corrosion behavior of Al alloys.

The alloys of this study contain coarse intermetallic particles with sizes in the range of 1-50 µm, known as constituent particles, Fig. 4. These particles were aligned along the deformation direction (as indicated by the red arrows), and were isolated or grouped, as shown in Fig. 5. These particles are formed during casting due to the low solubility of some elements, mainly Fe, in the Al matrix [71]. Besides Fe, elements as Al, Cu, and Mn, were also observed, Fig. 6. EDX maps show similarities and differences in the chemical composition of the particles in each alloy, Fig. 7. The relative weight percentages of Al, Cu, Fe, Mg, and Mn of the constituent particles were estimated based on the analysis of 70 individual particles, as indicated in Fig. 8. The dissimilarities in their compositions is explained by the different

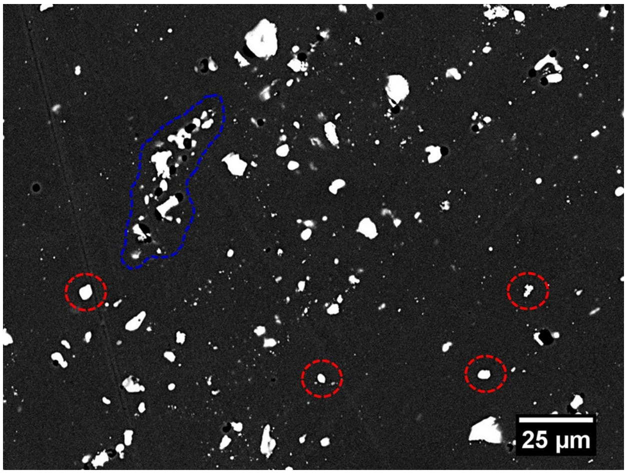

Fig. 5. Scanning electron micrograph of the 2024-T3 alloy surface showing constituent particles. The circulated regions red and blue indicate the particles isolated and grouped, respectively.

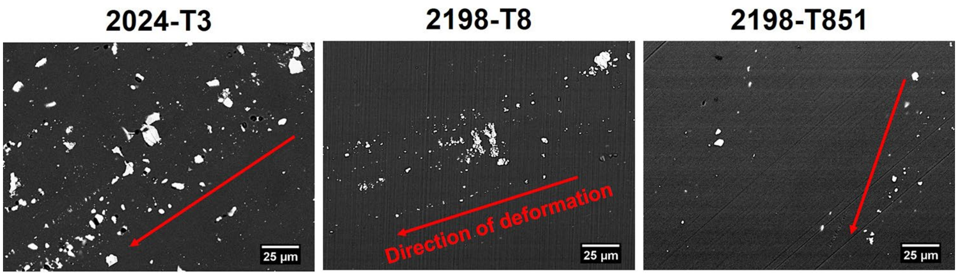
2024-T3
2198-T8
2198-T851

Fig. 4. Scanning electron micrographs showing the constituent particles present in the 2024-T3, 2198-T8, and 2198-T851 alloys.

Fig. 6. EDX spectrum of the constituent particles present in the 2024-T3, 2198-T8, and 2198-T851 alloys.

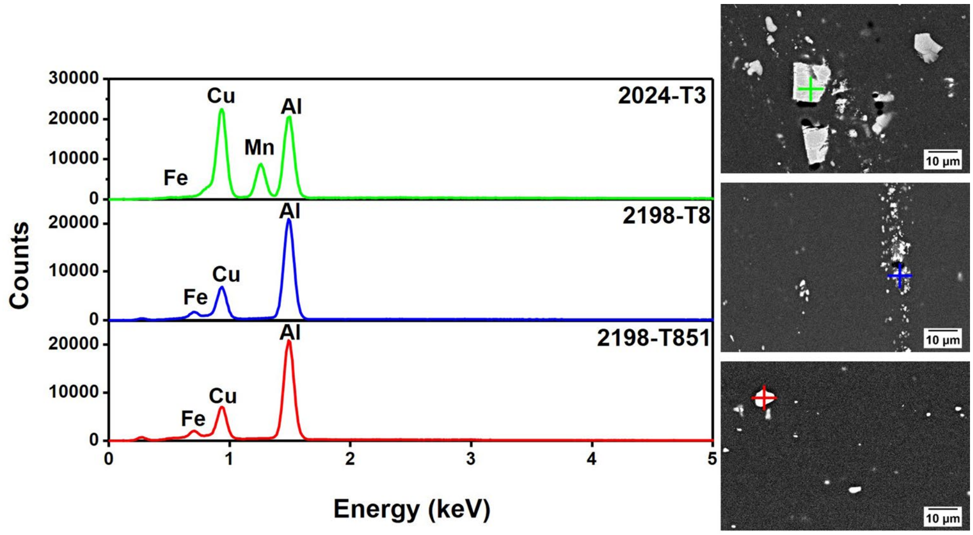

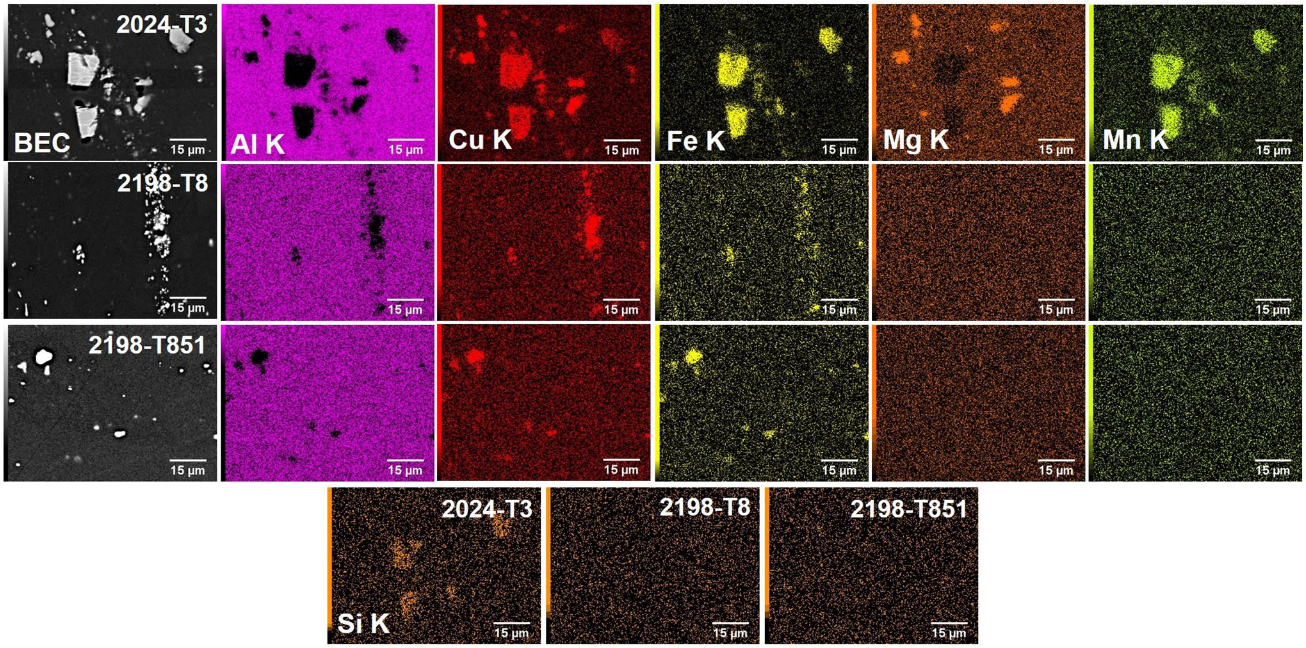

Fig. 7. EDX maps showing the distribution of elements of the constituent particles present in the 2024-T3, 2198-T8, and 2198-T851 alloys.

chemical composition of the alloys (Table 1). Table 4 shows the ratio between Cu and the main elements in the chemical composition of the studied alloys. The Cu/Mn ratio is inferior for the 2024 than for the 2198 alloys, due to the lower Mn content in the Al–Cu–Li alloys compared to the Al–Cu one. This explains the absence of Mn enriched micrometric particles in the 2198 alloys. Besides, Mg enrichment in the micrometric particles was only observed in the 2024 alloy despite the fact that the studied alloys presented similar Cu/Mg ratio. Also, the Cu/Fe ratio is higher in the 2198 alloys than in the 2024 but Fe was observed in the constituent particles of studied alloys due to its lower solubility in Al. Finally, the Al–Cu–Li alloys present similar Cu/Li ratio due to their similar chemical composition.

Each element is added to the alloy with specific purpose. Cu improves ductility and toughness; increases mechanical resistance by second phases precipitation and by solid solution; minimizes the formation of PFZ (precipitate-free zone); favors precipitation of high copper content micrometric particles during casting, and low copper content during aging [71]. Mg improves ductility, toughness, and the mechanical strength by precipitation of S phase (Al_2CuMg), as well as by solid solution, as shown in Fig. 6; decreases Li solubility and the alloy density. Li decreases density and

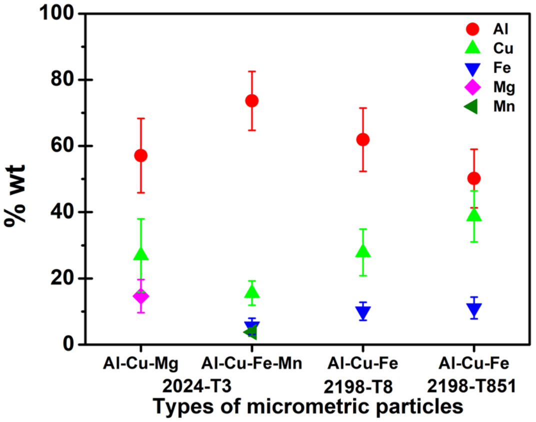

Fig. 8. Average weight percentages of elements present in 70 individual constituent particles.

Table 4. Weight elements ratio among the elements present in the chemical composition of alloys

Aluminum alloys	Relation among the elements			
	Cu/Mn	Cu/Mg	Cu/Fe	Cu/Li
2024-T3	9.23	8.16	34.28	–
2198-T8	> 100	10.78	83.5	3.56
2198-T851	> 100	10.68	82.75	3.45

increases mechanical resistance due to precipitation of T1 phase (Al_2CuLi) [72]. Mn controls grain size by precipitation of AlCuFeMn phases [65], as shown in Figs. 5 and 6. Fe and Si were found in the Al-alloys as impurities. They promote the formation of micrometric intermetallic phases (micro and nanosized), reduce density and indorse uniform plastic deformation [71]. Mn presents higher solubility in aluminum than Fe, explaining the absence of Mn enriched constituent particles in the 2198 tested alloys [71]. The histogram presented in Fig. 9 shows the distribution of the constituent particles size in the analyzed alloys. The statistical data is shown in Table 5. It is seen that the constituent particles in the 2024-T3 alloy present more varied sizes than the Al–Cu–Li alloys. The 2198-T8 and 2198-T851 present particles with similar range of sizes, as shown in Fig. 10. On the other hand, the number and percentage of particles per area varied for each alloy, as shown in Figs. 11 and 12.

The constituent particles are also known as intermetallics in the microstructure of the Al alloys. They are formed in the interdendritic regions during solidification or in the solid state during solution treatment, homogenization, or recrystallization and their formation is related to the alloying elements solubility in the Al alloys [73]. Si and Fe are impurities for the 2XXX series Al alloys and have low solubility in the Al matrix. Consequently, Fe- and Si-enriched coarse intermetallic compounds are commonly found in the

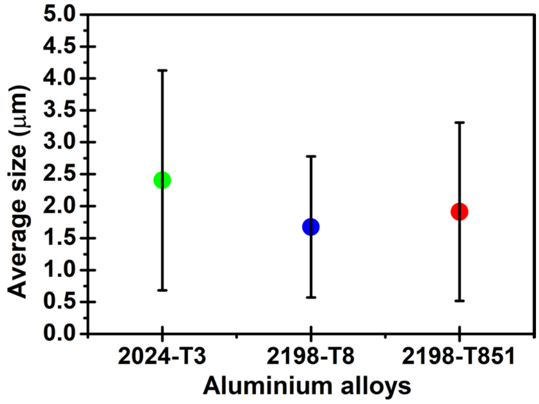

Fig. 9. Histogram of the constituent particle size distribution of the 2024-T3, 2198-T8, and 2198-T851 alloys.

Table 5. Statistical data of the average size of the constituent particles present in the alloys used in this study

Statistic data	Aluminum alloys		
	2024-T3	2198-T8	2198-T851
Mean	2.40	1.67	1.91
Standard deviation	1.71	1.10	1.39
Median	1.79	1.33	1.46
Mode	0.91	0.94	0.94
Minimum	0.91	0.92	0.95
Maximum	16.65	14	13.92
Count	2940	1771	523

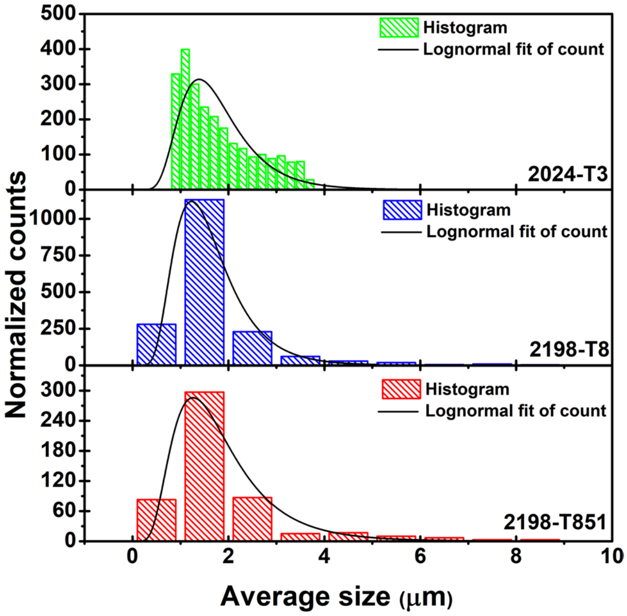

Fig. 10. Average constituent particle size present in the alloys used in this study obtained by the image analysis software.

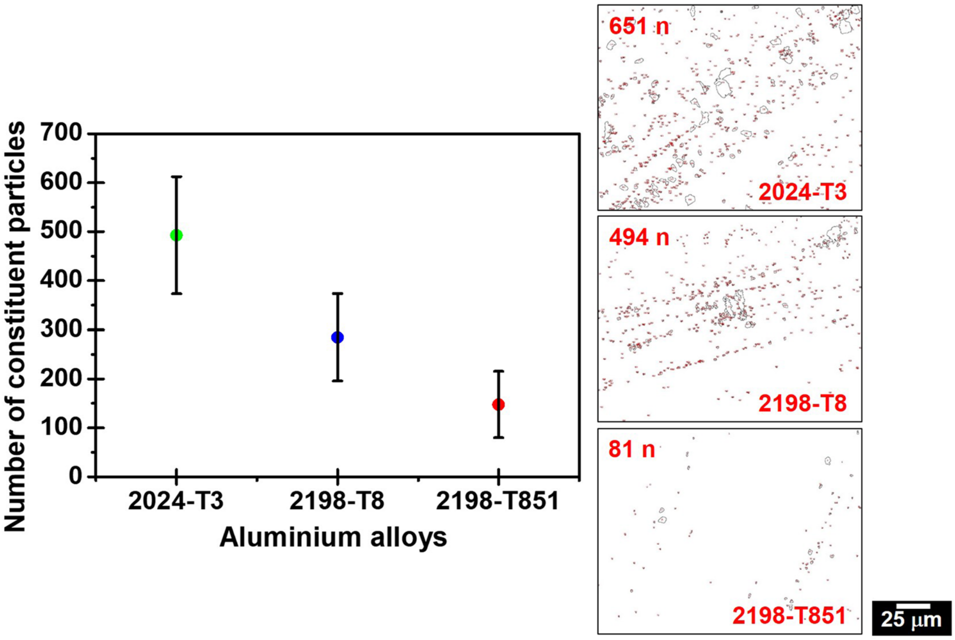

Fig. 11. The number of constituent particles present in the alloys used in this study obtained by the image analysis software.

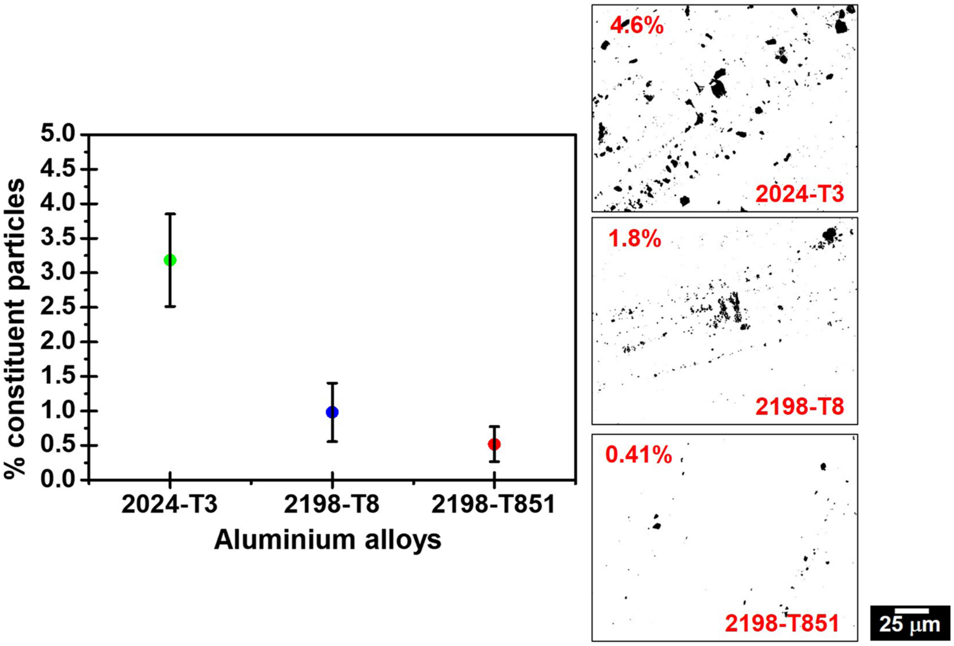

Fig. 12. Percentage of constituent particles present in the alloys used in this study obtained by the image analysis software.

2024 alloy. However, these intermetallics can consume other alloying elements during precipitation, such as Cu and Mg, and their nature depends on the solidification temperatures [74]. Each intermetallic has its nucleation and growth temperatures that can be seen in the alloy phase diagram. For instance, the higher amounts of Mg and Mn in the 2024-T3 alloy comparatively to the 2198 alloys tested resulted in growth and nucleation of Al–Fe–Cu–Mn and Al–Cu–Mg particles in the 2024 alloy. For the Al–Cu–Li alloys, the presence of Ag and Li favored precipitation of other particles, such as the Al–Cu and Al–Cu–Fe intermetallics observed. Also, it has been reported that traces of Ag and Mg in Al–Cu–Li alloys favor T1 phase precipitation kinetics; moreover, Ag also retarded the precipitation of S phase [75].

The 2024-T3 alloy presents the highest density and variety of particles among the tested ones. A comparison of the density of particles in the Al–Cu–Li alloys tested showed that the T8 alloy presented higher number of particles per area than the T851 alloy. It must be emphasized that the constituent particles have a negative effect on the corrosion resistance [21, 26, 27, 36–39, 51, 76–104] and on the electrochemical activity [49, 50, 105, 106] of the Al-alloys.

These particles, depending on their composition, act as cathodes or anodes relatively to the matrix. For instance, the 2024-T3 alloy contains particles with differences in their Cu-Fe contents. Thus, different oxidation behaviors are expected during anodizing of the 2024-T3 alloy compared with the 2198-T8 and 2198-T851 alloys [105]. The Fe-rich intermetallic compounds act as cathodes (nobler phase than matrix), whereas the S-phase as anode due to its Mg content [105].

Different morphology and sizes of intermetallic particles affect the corrosion behavior of Al alloys. According to Blanc and Mankowski [70] and Blanc et al. [77] the size and amount of particles in the 2024 alloy, besides their composition are among the most significant features influencing pitting properties. The passive film homogeneity decreased with increased size and number of intermetallic particles. Also, the composition of the particles has a strong effect on localized corrosion resistance. The Cu-enriched deposits that result from selective dissolution in Al–Cu–Mg intermetallics, besides the Cu deposition around these particles, alter the properties of the passive film resulting in a more conductive film, with the sites around the Cu-enriched particles of Cu deposits becoming preferential sites for pitting. For the 2198 alloys, pitting corrosion was mainly related to the nanometric T1 phase. Once the pitting occurs in the areas with higher density of T1 phase, it was related to grains of preferential orientation. The Al–Cu–Fe particles are cathodic to the matrix and represent a lower influence on pitting corrosion than the T1 anodic phase relatively to the matrix. Besides, a high density of constituent particles leads to imperfect anodized layers [51, 107]. Consequently, surface pretreatments, prior to anodizing, is important, mainly for the 2024-T3 alloy when compared to the 2198 alloys used in this study.

It is important to point out that the constituent particles do not contribute to the mechanical properties of Al alloys [108]. However, the hardening phases which precipitate during aging treatments increase the mechanical properties. These phases are mainly the S (Al_2CuMg) and the T1 (Al_2CuLi) phases for the Al–Cu and Al–Cu–Li alloys, respectively. Microhardness results for the alloys of this study are shown in Fig. 13a. The 2198-T8 alloy presented microhardness nearly 36 $HV_{0.3}$ higher than that of the 2024-T3. For the 2198-T851, different microhardness values were measured in the grains with or without slip bands, as shown Figs. 13b,c. The microhardness was approximately 25.7 $HV_{0.3}$ higher for the grains with slip bands. Once the slip bands are preferential sites for nucleation of T1 phase [109], these grains have higher densities of T1 phase. This was supported by observation of surface during etching. Preferential attack of the T1 phase revealed the slip bands, as shown in Figs. 1, 2, and 13b,c.

As mentioned, the main hardening phase in Al–Cu–Li alloys is the T1 phase, Fig. 14. In the 2024-T3 alloy, the S (Al_2CuMg) and θ (Al_2Cu) phases are the main hardening precipitates [110, 111]. The S phase is found in micro and nanoscale as coarse intermetallic particles, Fig. 6, or fine precipitates [111]. The fine precipitates are responsible for increased mechanical resistance. Also, in the 2024 alloy, second phases with variable stoichiometry, composed of Al–Cu–Fe–Mn–(Si) and Al–Cu–Mn, are commonly found, Figs. 15 and 16. In Table 6, the nanometric particles showed in Fig. 15 are identified. Nanometric phases enriched in Cu and Fe and with Ag at their borders were found in the Al–Cu–Li alloys, Fig. 17. Addition of Zr in Al–Cu–Li alloys leads to precipitation of Cu–Fe–Zr enriched nanometric phases, Fig. 18. Ag increases ductility and toughness; favors stabilization of subgrains

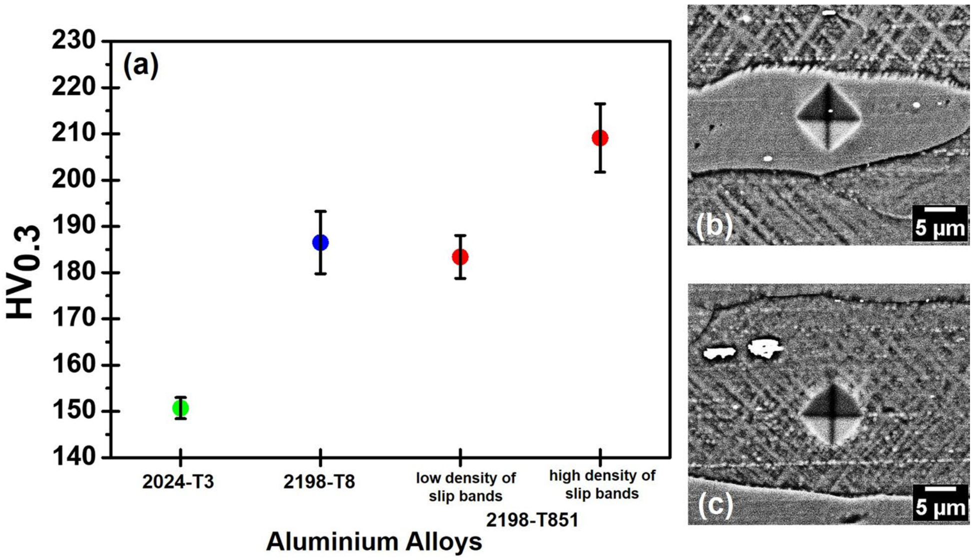

Fig. 13. **a** Microhardness measurements of the alloys used in this study and Microhardness measurements in grains of **b** low density and **c** high density of slip bands in the 2198-T851 alloy.

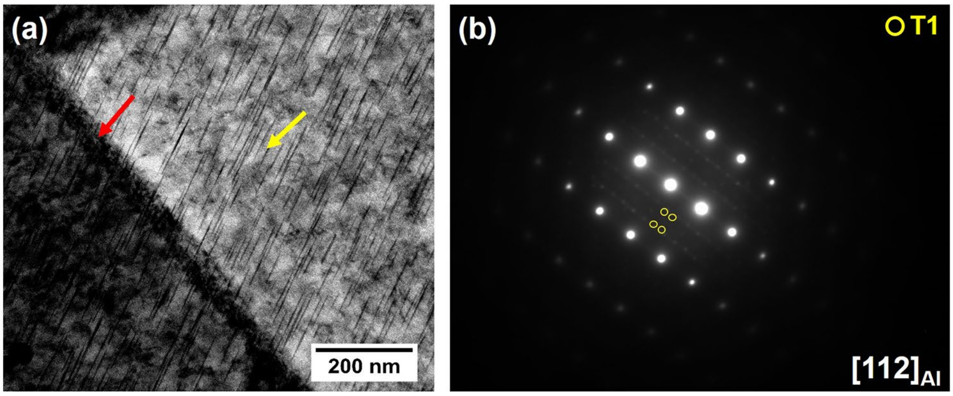

Fig. 14. **a** Bright-field TEM micrograph of the Al–Cu–Li alloy, and **b** diffraction pattern of the selected area (SAED). The arrows red and yellow represented the grains boundaries and T1 phase.

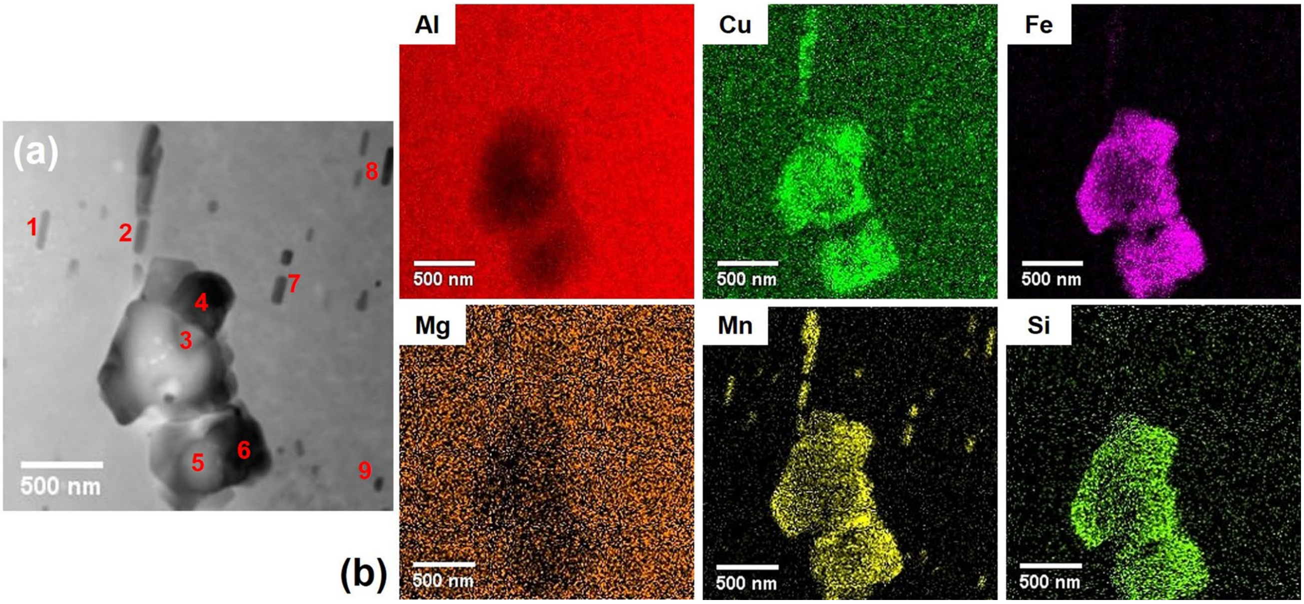

Fig. 15. **a** Bright-field image of the 2024-T3 alloy, **b** EDX maps showing the distribution of Al, Cu, Fe, Mg, Mn, and Si.

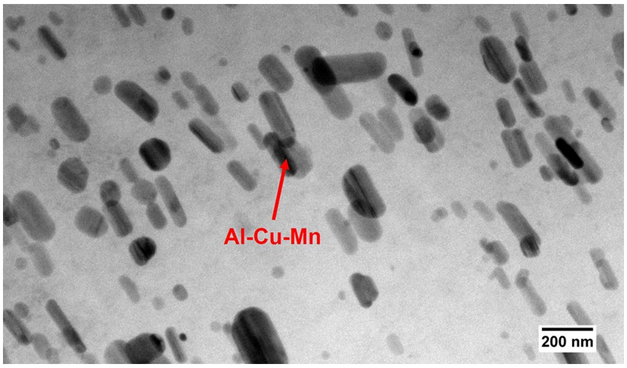

Fig. 16. Bright-field image TEM of the 2024-T3 alloy showing the presence of Al–Cu–Mn phases.

and delays recrystallization [112]. Al–Cu–Fe enriched intermetallics are mostly found at the grain boundaries, whereas Al–Cu–Zr precipitates are confined inside the grains [4].

Once the 2198 was developed to replace the 2024-T3 alloys in aircraft structures, their mechanical properties have been compared in the literature. It was observed that the differences between these alloys' properties are dependent on their thermomechanical process conditions. For instance, it has been reported that when both kinds of alloys are naturally aged, the 2024 present better mechanical properties than the 2198 [30, 113, 114]. On the other hand, when the 2198 is artificially aged or stretched its

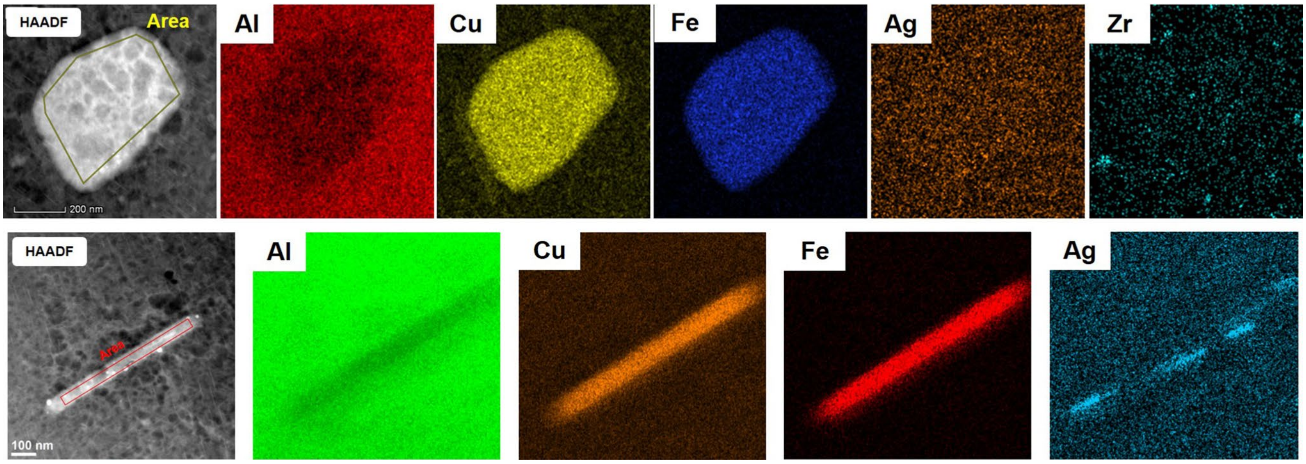

Fig. 17. EDX maps showing the distribution of elements of the Al–Cu–Fe type nanometric particles present in the Al–Cu–Li alloys.

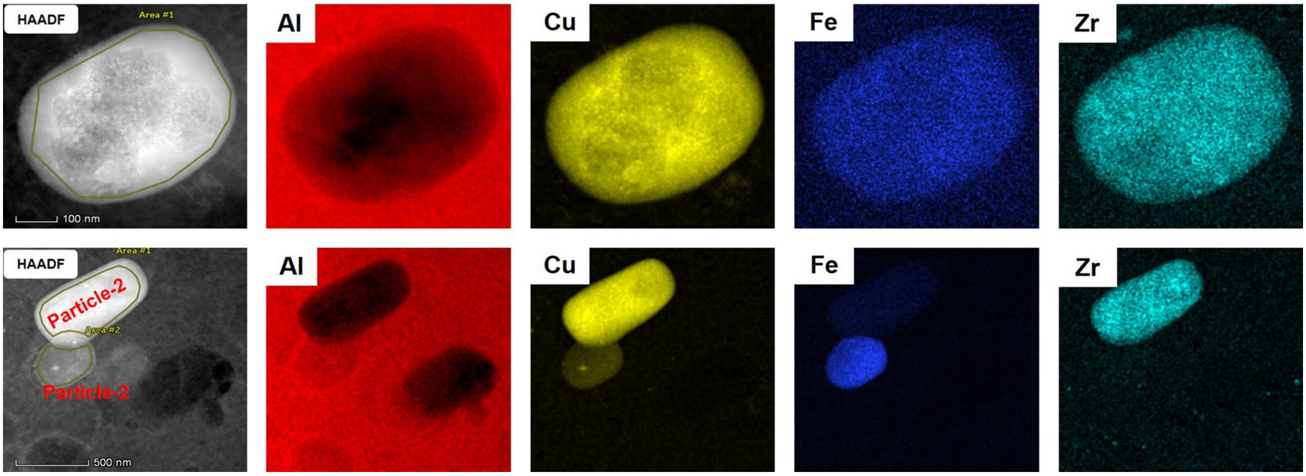

Fig. 18. EDX maps showing the distribution of elements of the Al–Cu–Zr type nanometric particles present in the Al–Cu–Li alloys.

mechanical properties, as toughness and fatigue life time, are superior to the 2024-T3 alloy for aircraft applications [28, 115]. These observations are in agreement with the microhardness results where the 2198-T8 and 2198-T851 alloys showed higher hardness values than the 2024-T3.

It is important to note that the S (Mg-rich) and T1 (Li-rich) phases present distinct electrochemical behaviors, as reported in previous work [116]. Both elements, Mg and Li, are extremely reactive when compared to other alloying elements in the Al alloys [116]. However, the T1 phase has a potential − 0.2 V inferior, when compared to that of the S phase [82]. The distinct nature of these phases leads to different types of corrosion attacks. The T1 phase promotes crystallographic attack and severe localize corrosion (SLC) [109], whereas, S phase leads to intergranular corrosion [38].

Table 6 Information about the nanometric particles present in 2024-T3 shown in Fig. 15.

Particle	Dominant composition	Phases
1	Al–Cu–Mn	Dispersoids
2	Al–Cu–Mn	Dispersoids
3	Al–Cu	θ phase
4	Al–Cu–Fe–Mn–Si	Second phase
5	Al–Cu	θ phase
6	Al–Cu–Fe–Mn–Si	Second phase
7	Al–Cu–Mn	Dispersoids
8	Al–Cu–Mn	Dispersoids
9	Al–Cu–Mn	Dispersoids

The dissimilarities among Al–Cu–Mg and Al–Cu–Li alloys still provide many challenges for materials engineering. Complex metallurgical microstructures may be obtained in Al-alloys as a result of casting, homogenization, and subsequent thermomechanical processing. These processes change the alloy microstructure, and consequently, the mechanical and corrosion resistance properties. Few modifications in the manufacturing process may change the alloy microstructure. Consequently, studies on the microstructure evolution must be carried out to improve the knowledge on the correlation between processing and microstructure.

Conclusion

The microstructures of the Al–Cu–Mg and Al–Cu–Li alloys used in this study were investigated and the differences observed were correlated with their chemical composition and thermomechanical processing. The main hardening phases in the Al–Cu–Mg (2024-T3) and Al–Cu–Li (2198-T8 and 2198-T851) alloys are the Mg-enriched S-phase and Li-enriched T1-phase, respectively. The 2024-T3 alloy presented two main types of constituent particles, specifically, Al–Cu–Mg and Al–Cu–Mn-Fe–(Si), whereas the 2198-T8 and 2198–T851 alloys showed only one type of constituent particle, composed of Al–Cu–Fe. Higher density of constituent particles was related to the 2024-T3 comparatively to the 2198-T8 and 2198-T851. Microhardness results, on the other hand, indicated higher amounts of hardening nanometric precipitates in the 2198 alloys comparatively to the 2024-T3 which was related to artificial aging in the 2198 alloys whereas natural aging in the 2024 one. Finally, the T851 temper showed slip bands inside some grains, which were attributed to the stretching stage that is part of this treatment and resulted in preferential attack of the slip bands during chemical etching.

Acknowledgments The authors acknowledge CNPq (426280-2016-4) and FAPESP (2013/13235-6) for financial support to this work and are thankful to FAPESP (2019/18388-1) for the Grant of João Victor de Sousa Araujo.

References

1. J.C. Williams, E.A. Starke, Progress in structural materials for aerospace systems. Acta Mater. **51**, 5775–5799 (2003)
2. R. Lumley, *Fundamentals of Aluminium Metallurgy*, 1st edn. (Elsevier, London, 2018)
3. R.J. Rioja, J. Liu, The evolution of Al–Li base products for aerospace and space applications. Metall. Mater. Trans. A Phys. Metall. Mater. Sci. **43**, 3325–3333 (2012)
4. T. Dorin, A. Vahid, J. Lamb, *Aluminium Lithium Alloys in Fundamentals of Aluminium Metallurgy* (Elsevier, London, 2018), pp. 387–438
5. A. Gloria, R. Montanari, M. Richetta, A. Varone, Alloys for aeronautic applications: state of the art and perspectives. Metals (Basel). **662**, 1–26 (2019)
6. A.P. Mouritz (ed.), Aerospace materials: past, present and future, in Introduction to Aerospace Materials (Elsevier, London, 2012), pp. 15–38
7. A.P. Mouritz (ed.), Materials and material requirements for aerospace structures and engines, in *Introduction to Aerospace Materials*. (Elsevier, London, 2012), pp. 39–56
8. P. Rambabu, N. Eswara Prasad, V.V. Kutumbarao, R.J.H. Wanhill, *Aluminium Alloys for Aerospace Applications*, 1st edn. (Springer, Singapore, 2017)
9. A.P. Mouritz (ed.), Aluminium alloys for aircraft structure, in *Introduction to Aerospace Materials*. (Elsevier, London, 2012), pp. 173–201
10. N. Eswara Prasad, A. Gokhale, R.J.H. Wanhill, *Aluminum–Lithium Alloys*, 1st edn. (Elsevier, London, 2014)
11. O. Grushko, B. Ovsyannikov, V. Ovchinnokov, *Aluminum–Lithium Alloys: Process Metallurgy, Physical Metallurgy, and Welding*, 1st edn. (CRC Press, London, 2016)
12. S.C. Wang, M.J. Starink, Precipitates and intermetallic phases in precipitation hardening Al–Cu–Mg–(Li) based alloys. Int. Mater. Rev. **50**, 193–215 (2005)
13. T. Dursun, C. Soutis, Recent developments in advanced aircraft aluminium alloys. Mater. Des. **56**, 862–871 (2014)
14. R.J.H. Wanhill, *Aerospace Applications of Aluminum–Lithium Alloys*, 1st edn. (Butterworth-Heinemann, London, 2013)
15. C. Vargel, *Corrosion of Aluminium*, 1st edn. (Elsevier, London, 2013)
16. C. Gao, Y. Ma, L. Zhi Tang, P. Wang, X. Zhang, Microstructural evolution and mechanical behavior of friction spot welded 2198-T8 Al–Li alloy during aging treatment. Mater. Des. **115**, 224–230 (2017)
17. B. Han, Y. Chen, W. Tao, H. Li, L. Li, Microstructural evolution and interfacial crack corrosion behavior of double-sided laser beam welded 2060/2099 Al–Li alloys T-joints. Mater. Des. **135**, 353–365 (2017)
18. P. Zhu, Y. Ma, K. Li, Z. Liang, B. Yang, W. Huang, Y. Liao, Sealing of anodized AA2099-T83 Al–Cu–Li alloy with layered double hydroxides for high corrosion resistance at reduced anodic film thickness. Surf. Coat. Technol. **394**, 125852 (2020)
19. J.V. de Sousa Araujo, A.F. de Santos Bugarin, U. Donatus, C.S.C. de Machado, F.M. Queiroz, M. Terada, A. Astarita, I. Costa, Thermomechanical treatment and corrosion resistance correlation in the AA2198 Al–Cu–Li alloy. Corros. Eng. Sci. Technol. **2782**, 575–586 (2019)
20. Y.-L. Ma, X.-R. Zhou, X.-M. Meng, W.-J. Huang, Y. Liao, X.-L. Chen, Y.-N. Yi, X.-X. Zhang, G.E. Thompson, Influence of thermomechanical treatments on localized corrosion susceptibility and propagation mechanism of AA2099 Al–Cu–Li alloy. Trans. Nonferrous Met. Soc. China **26**, 1472–1481 (2016)
21. X. Zhou, C. Luo, Y. Ma, T. Hashimoto, G.E. Thompson, A.E. Hughes, P. Skeldon, Grain-stored energy and the propagation of intergranular corrosion in AA2XXX aluminium alloys. Surf. Interface Anal. **45**, 1543–1547 (2013)
22. T. Sheppard, N.C. Parson, Corrosion resistance of Al–Li alloys. Mater. Sci. Technol. **3**, 345–352 (1987)
23. X. Zhang, X. Zhou, T. Hashimoto, B. Liu, Localized corrosion in AA2024-T351 aluminium alloy: transition from intergranular corrosion to crystallographic pitting. Mater. Charact. **130**, 230–236 (2017)
24. J.V. Sousa Araujo, M.X. Milagre, R.O. Ferreira, C. Souza Carvalho Machado, A. Fátima Santos Bugarin, I.F. Machado, I. Costa, Exfoliation and intergranular corrosion resistance of the 2198 Al–Cu–Li alloy with different thermomechanical

treatments. Mater. Corros. (2020). https://doi.org/10.1002/maco.202011839

25. M.X. Milagre, U. Donatus, C.S.C. Machado, J.V.S. Araujo, R.M.P. da Silva, B.V.G. de Viveiros, A. Astarita, I. Costa, Comparison of the corrosion resistance of an Al–Cu alloy and an Al–Cu–Li alloy. Corros. Eng. Sci. Technol. **54**, 402–412 (2019)
26. J.A. Moreto, C.E.B. Marino, W.W. Bose Filho, L.A. Rocha, J.C.S. Fernandes, SVET, SKP and EIS study of the corrosion behaviour of high strength Al and Al–Li alloys used in aircraft fabrication. Corros. Sci. **84**, 30–41 (2014)
27. J.A. Moreto, O.C. Gamboni, C.E.B. Marino, W. Bose Filho, J.C.S. Fernandes, L.A. Rocha, Corrosion behaviour of Al and Al–Li alloys used as aircraft materials. Corros. Prot. Mater **31**, 60–64 (2012)
28. N.D. Alexopoulos, E. Migklis, A. Stylianos, D.P. Myriounis, Fatigue behavior of the aeronautical Al–Li (2198) aluminum alloy under constant amplitude loading. Int. J. Fatigue **56**, 95–105 (2013)
29. N.D. Alexopoulos, A. Proiou, T. Examilioti, N. Kashaev, S. Riekehr, S.K. Kourkoulis, Effect of artificial aging on the mechanical performance of (Al–Cu) 2024 and (Al–Cu–Li) 2198 aluminum alloys. Proced. Struct. Integr. **2**, 3782–3783 (2016)
30. N.D. Alexopoulos, A. Proiou, W. Dietzel, C. Blawert, V. Heitmann, M. Zheludkevich, S.K. Kourkoulis, Mechanical properties degradation of (Al–Cu–Li) 2198 alloy due to corrosion exposure. Proced. Struct. Integr. **2**, 597–603 (2016)
31. P. Lequeu, K.P. Smith, A. Daniélou, Aluminum–copper–lithium alloy 2050 developed for medium to thick plate. J. Mater. Eng. Perform. **19**, 841–847 (2010)
32. C.P. Blankenship, E.A. Starke, The fatigue crack growth behavior of the Al–Cu–Li alloy weldalite. Fatigue Fract. Eng. Mater. Struct. **14**, 103–114 (1991)
33. C.P. Dervenis, E.I. Meletis, R.F. Hochman, Corrosion fatigue in Al-Li alloy 2090. Mater. Sci. Eng. **102**, 151–160 (1988)
34. J.A. Moreto, O. Gamboni, C.O.F.T. Rucherf, F. Romagnoli, M.F. Moreira, F. Beneduce, W.W. Bose Filho, Corrosion and fatigue behavior of new Al alloys. Proced. Eng. **10**, 1521–1526 (2011)
35. J.A. Moreto, E.E. Broday, L.S. Rossino, J.C.S. Fernandes, W.W. Bose Filho, Effect of localized corrosion on fatigue-crack growth in 2524–T3 and 2198–T851 aluminum alloys used as aircraft materials. J. Mater. Eng. Perform. **27**, 1917–1926 (2018)
36. A. Boag, A. Hughes, A. Glenn, Corrosion of AA2024-T3 part I: localised corrosion of isolated IM particles. Corros. Sci. **53**, 17–26 (2011)
37. A. Hughes, A. Boag, A. Glenn, Corrosion of AA2024-T3 part II: co-operative corrosion. Corros. Sci. **53**, 27–39 (2011)
38. A. Glenn, T. Muster, C. Luo, X. Zhou, G.E. Thompson, A. Boag, A.E. Hughes, Corrosion of AA2024-T3 part III: propagation. Corros. Sci. **53**, 40–50 (2011)
39. J.A. Moreto, L.S. Rossino, W.W.B. Filho, C.E.B. Marino, M. Da Conceição Ferreira, M. Taryba, J.C.S. Fernandes, On the global and localised corrosion behaviour of the AA2524-T3 aluminium alloy used as aircraft fuselage skin. Mater. Res. **22** (2019). https://doi.org/10.1590/1980-5373-mr-2018-0280
40. X. Zhou, C. Luo, T. Hashimoto, A.E. Hughes, G.E. Thompson, Study of localized corrosion in AA2024 aluminium alloy using electron tomography. Corros. Sci. **58**, 299–306 (2012)
41. M.X. Milagre, N.V. Mogili, U. Donatus, R.A.R. Giorjão, M. Terada, J.V.S. Araujo, C.S.C. Machado, I. Costa, On the microstructure characterization of the AA2098-T351 alloy welded by FSW. Mater. Charact. **140**, 233–246 (2018)
42. R. Walter, M.B. Kannan, Influence of surface roughness on the corrosion behaviour of magnesium alloy. Mater. Des. **32**, 2350–2354 (2011)
43. M.B. Leban, Č Mikyška, T. Kosec, B. Markoli, J. Kovač, The effect of surface roughness on the corrosion properties of type AISI 304 stainless steel in diluted NaCl and urban rain solution. J. Mater. Eng. Perform. **23**, 1695–1702 (2014)
44. J.G. Kaufman, *Properties of Aluminum Alloys: Fatigue Data and the Effects of Temperature, Product Form, and Processing*, 1st edn. (ASM International, London, Materials Park, 2014)
45. S.B. Prabu, K.A. Padmanabhan, Superplasticity in and Superplastic Forming of Aluminum-Lithium Alloys, in *Aluminum–lithium Alloys*, ed. By N. Eswara Prasad, A. Gokhale, R.J.H. Wanhill (Elsevier, UK, 2013), pp. 221–258
46. M.M. Attallah, H.G. Salem, Influence of process parameters on superplasticity of friction stir processed nugget in high strength Al–Cu–Li alloy. Mater. Sci. Technol. **20**, 1370–1376 (2004)
47. N. Eswara Prasad, T.S. Srivatsan, R.J.H. Wanhill, G. Malakondaiah, V.V. Kutumbarao, Fatigue behavior of aluminum–lithium alloys, in *Aluminum–Lithium Alloys*, ed. By N. Eswara Prasad, A. Gokhale, R.J.H. Wanhill (Elsevier, UK, 2013), pp. 341–379
48. M. Saenz de Miera, M. Curioni, P. Skeldon, G.E. Thompson, The behaviour of second phase particles during anodizing of aluminium alloys. Corros. Sci. **52**, 2489–2497 (2010)
49. Y. Ma, X. Zhou, G.E. Thompson, M. Curioni, X. Zhong, E. Koroleva, P. Skeldon, P. Thomson, M. Fowles, Discontinuities in the porous anodic film formed on AA2099-T8 aluminium alloy. Corros. Sci. **53**, 4141–4151 (2011)
50. Y. Ma, X. Zhou, K. Li, S. Pawar, Y. Liao, Z. Jin, Z. Wang, H. Wu, Z. Liang, L. Liu, Corrosion and anodizing behavior of $T_1(Al_2CuLi)$ precipitates in Al–Cu–Li alloy. J. Electrochem. Soc. **166**, C296–C303 (2019)
51. Y. Ma, H. Wu, X. Zhou, K. Li, Y. Liao, Z. Liang, L. Liu, Corrosion behavior of anodized Al–Cu–Li alloy: the role of intermetallic particle-introduced film defects. Corros. Sci. **158**, 108110 (2019). https://doi.org/10.1016/j.corsci.2019.108110
52. J. Liu, G. Rong, S. Cen, S. Li, H. Shi, K. Zhao, M. Yu, Dissolution behavior of intermetallic particles in AA2297-T87 during anodizing in adipic-sulfuric acid. J. Electrochem. Soc. **165**, C980–C990 (2018)
53. M. Curioni, F. Roeth, S.J. Garcia-Vergara, T. Hashimoto, P. Skeldon, G.E. Thompson, J. Ferguson, Enrichment, incorporation and oxidation of copper during anodising of aluminium–copper alloys. Surf. Interface Anal. **42**, 234–240 (2010)
54. F.M. Queiroz, U. Donatus, O.M. Ramirez, J.V. de Sousa Araujo, B.V. de Viveiros, S. Lamaka, M. Zheludkevich, M. Masoumi, V. Vivier, I. Costa, H.G. de Melo, Effect of unequal levels of deformation and fragmentation on the electrochemical response of friction stir welded AA2024-T3 alloy. Electrochim. Acta. **313**, 271–281 (2019)
55. R. Saillard, B. Viguier, G. Odemer, A. Pugliara, B. Fori, C. Blanc, Influence of the microstructure on the corrosion behaviour of 2024 aluminium alloy coated with a trivalent chromium conversion layer. Corros. Sci. **142**, 119–132 (2018)
56. C. Luo, S.P. Albu, X. Zhou, Z. Sun, X. Zhang, Z. Tang, G.E. Thompson, Continuous and discontinuous localized corrosion of a 2XXX aluminium–copper–lithium alloy in sodium chloride solution. J. Alloys Compd. **658**, 61–70 (2016)
57. A. Balbo, A. Frignani, V. Grassi, F. Zucchi, Electrochemical behaviour of AA2198 and AA2139 in neutral solutions. Mater. Corros. **66**, 796–802 (2015)
58. J.V. de Sousa Araujo, U. Donatus, F.M. Queiroz, M. Terada, M.X. Milagre, M.C. de Alencar, I. Costa, On the severe localized corrosion susceptibility of the AA2198-T851 alloy. Corros. Sci. **133**, 132–140 (2018)
59. M.X. Milagre, U. Donatus, C.S.C. Machado, J.V.S. Araujo, R.O. Ferreira, R.M.P. Silva, R.A. Antunes, L. Costa, Exfoliation corrosion susceptibility in the zones of friction stir welded AA2098-T351. J. Mater. Res. Technol. **8**, 5916–5929 (2019)

60. A.E. Hughes, N. Birbilis, J.M. Mol, S.J. Garcia, X. Zhou, G.E. Thompson, Corrosion and principles of protection, in *Recent Trends Process. Degrad. Alum. Alloy* (InTech, 2011), pp. 223–262. https://doi.org/10.5772/18766
61. J.C. Benedyk, International temper designation systems for wrought aluminium alloys: part II—thermally treated (T temper) aluminium alloys. Light Met. Age. 16–22 (2010)
62. N. Hansen, D.J. Jensen, Development of microstructure in FCC metals during cold work. Philos. Trans. R. Soc. A Math. Phys. Eng. Sci. **357**, 1447–1469 (1999)
63. K.V. Jata, A.K. Singh, Texture and its effects on properties in aluminum–lithium alloys, in *Aluminum–Lithium Alloy, Process. Prop. Appl.* (Elsevier, UK, 2013), pp. 139–163
64. H.Y. Hollingsworth, E.H. Hunsciker, P.A. Schweitzer, *Aluminium Alloys in Corrosion and Corrosion Protection Handbook*, p.135 (1983). https://doi.org/10.31399/asm.hb.v13b.a0003815
65. T. Arai, Heat treating of aluminum alloys, in *ASM Handbook* (UK, 1990), pp. 841–879. https://doi.org/10.1361/asmhba000
66. K.D. Ralston, D. Fabijanic, N. Birbilis, Effect of grain size on corrosion of high purity aluminium. Electrochim. Acta **56**, 1729–1736 (2011)
67. G. Jeong, J. Park, S. Nam, S.E. Shin, J. Shin, D. Bae, H. Choi, The effect of grain size on the mechanical properties of aluminum. Arch. Metall. Mater. **60**, 1287–1291 (2015)
68. B.L. Adams, *ASM Handbook Properties and Selection: Nonferrous Alloys and Special-Purpose Materials* (American Society for Materials, Estados Unidos de América, 2001) https://doi.org/10.1016/S0026-0576(03)90166-8
69. D. Yin, H. Liu, Y. Chen, D. Yi, B. Wang, B. Wang, F. Shen, S. Fu, C. Tang, S. Pan, Effect of grain size on fatigue-crack growth in 2524 aluminium alloy. Int. J. Fatigue **84**, 9–16 (2016)
70. C. Blanc, G. Mankowski, Susceptibility to pitting corrosion of 6056 aluminium alloy. Corros. Sci. **39**, 949–959 (1997)
71. N.A. Belov, D.G. Eskin, A.A. Aksenov, *Multicomponent Phase Diagrams*, 1st edn. (Elsevier, London, 2005)
72. J. Li, P. Liu, Y. Chen, X. Zhang, Z. Zheng, Microstructure and mechanical properties of Mg, Ag and Zn multi-microalloyed Al–(3.2–3.8)Cu–(1.0–1.4)Li alloys. Trans. Nonferrous Met. Soc. China **25**, 2103–2112 (2015)
73. W.S. Ebhota, T.-C. Jen, Intermetallics formation and their effect on mechanical properties of Al–Si–X alloys, in *Intermetallic Compounds—Formation and Applications*, ed. By M. Aliofkhazraei (InTech, 2018). https://doi.org/10.5772/intechopen.73188
74. S.G. Shabestari, M.H. Ghoncheh, H. Momeni, Evaluation of formation of intermetallic compounds in Al2024 alloy using thermal analysis technique. Thermochim. Acta **589**, 174–182 (2014)
75. B.P. Huang, Z.Q. Zheng, Independent and combined roles of trace Mg and Ag additions in properties precipitation process and precipitation kinetics of Al–Cu–Li–(Mg)–(Ag)–Zr–Ti alloys. Acta Mater. **46**, 4381–4393 (1998)
76. Y. Ma, X. Zhou, W. Huang, G.E. Thompson, X. Zhang, C. Luo, Z. Sun, Localized corrosion in AA2099-T83 aluminum–lithium alloy: the role of intermetallic particles. Mater. Chem. Phys. **161**, 201–210 (2015)
77. C. Blanc, B. Lavelle, G. Mankowski, The role of precipitates enriched with copper on the susceptibility to pitting corrosion of the 2024 aluminium alloy. Corros. Sci. **39**, 495–510 (1997)
78. L. Lacroix, L. Ressier, C. Blanc, G. Mankowski, Combination of AFM, SKPFM, and SIMS to study the corrosion behavior of S-phase particles in AA2024-T351. J. Electrochem. Soc. **155**, 131–137 (2008)
79. M. Guérin, E. Andrieu, G. Odemer, J. Alexis, C. Blanc, Effect of varying conditions of exposure to an aggressive medium on the corrosion behavior of the 2050 Al–Cu–Li alloy. Corros. Sci. **85**, 455–470 (2014)
80. C. Larignon, J. Alexis, E. Andrieu, L. Lacroix, G. Odemer, C. Blanc, Combined Kelvin probe force microscopy and secondary ion mass spectrometry for hydrogen detection in corroded 2024 aluminium alloy. Electrochim. Acta **110**, 484–490 (2013)
81. C.M. MacRae, A.E. Hughes, J.S. Laird, A.M. Glenn, N.C. Wilson, A. Torpy, M.A. Gibson, X. Zhou, N. Birbilis, G.E. Thompson, An examination of the composition and microstructure of coarse intermetallic particles in AA2099-T8. Microsc. Microanal. **24**, 325–341 (2018)
82. R.G. Buchheil, A compilation of corrosion potentials reported for intermetallic phases in aluminium alloys. J. Electrochem. Soc. **142**, 3994–3996 (1995)
83. N. Birbilis, R.G. Buchheit, Electrochemical characteristics of intermetallic phases in aluminum alloys. J. Electrochem. Soc. **152**, B140 (2005)
84. R.G. Buchheit, J.P. Moran, G.E. Stoner, Localized corrosion behavior of alloy 2090—the role of microstructural heterogeneity. Corrosion **46**, 610–617 (1990)
85. R.G. Buchheit, Local dissolution phenomena associated with S phase (Al_2CuMg) particles in aluminum alloy 2024–T3. J. Electrochem. Soc. **144**, 2621 (1997)
86. E. Ghanbari, A. Saatchi, X. Lei, D.D. Macdonald, Studies on pitting corrosion of Al–Cu–Li alloys part II: breakdown potential and pit initiation. Materials (Basel). **12**, 1786 (2019)
87. Y. Zhu, K. Sun, G.S. Frankel, Intermetallic phases in aluminum alloys and their roles in localized corrosion. J. Electrochem. Soc. **165**, C807 (2018)
88. R. Grilli, M.A. Baker, J.E. Castle, B. Dunn, J.F. Watts, Localized corrosion of a 2219 aluminium alloy exposed to a 3.5% NaCl solution. Corros. Sci. **52**, 2855–2866 (2010)
89. X. Lei, A. Saatchi, E. Ghanbari, R. Dang, W. Li, N. Wang, D.D. Macdonald, Studies on pitting corrosion of Al–Cu–Li alloys part I: effect of Li addition by microstructural. Materials (Basel). **12**, 1600 (2019)
90. E. Ghanbari, A. Saatchi, X. Lei, D.D. Macdonald, Studies on pitting corrosion of Al–Cu–Li alloys part III: passivation kinetics of AA2098–T851 based on the point defect model. Materials (Basel). **12**, 1912 (2019)
91. Y. Long Ma, X. Rong Zhou, X. Min Meng, W. Jiu Huang, Y. Liao, X. Li Chen, Y. Nan Yi, X. Xin Zhang, G.E. Thompson, Influence of thermomechanical treatments on localized corrosion susceptibility and propagation mechanism of AA2099 Al–Li alloy. Trans. Nonferrous Met. Soc. China. **26**, 1472–1481 (2016)
92. F.M. Queiroz, H.G. De Melo, I. Costa, Effect of intermetallics on the corrosion of Al 2024–T3 alloy in solutions with different chloride concentration. Mater. Sci. Forum **587–588**, 415–419 (2008)
93. F.M. Queiroz, M. Magnani, I. Costa, H.G. de Melo, Investigation of the corrosion behaviour of AA 2024-T3 in low concentrated chloride media. Corros. Sci. **50**, 2646–2657 (2008)
94. L. Yin, Y. Jin, C. Leygraf, N. Birbilis, J. Pan, Numerical simulation of micro-galvanic corrosion in Al alloys: effect of geometric factors. J. Electrochem. Soc. **164**, C75 (2017)
95. A.M. Glenn, A.E. Hughes, C.M. MacRae, N.C. Wilson, A. Torpy, X. Zhou, Observations on the early stages of corrosion on AA2099-T83. Microsc. Microanal. **26**, 821–836 (2020)
96. R. Ambat, A.J. Davenport, G.M. Scamans, A. Afseth, Effect of iron-containing intermetallic particles on the corrosion behaviour of aluminium. Corros. Sci. **48**, 3455–3471 (2006)
97. C. Örnek, C. Leygraf, J. Pan, Real-time corrosion monitoring of aluminum alloy using scanning kelvin probe force microscopy. J. Electrochem. Soc. **167**, 081502 (2020)
98. Y. Zhu, K. Sun, J. Garves, L.G. Bland, J. Locke, J. Allison, G.S. Frankel, Micro- and nano-scale intermetallic phases in AA2070-T8 and their corrosion behavior. Electrochim. Acta **319**, 634–648 (2019)

99. C.F. Mallinson, P.M. Yates, M.A. Baker, J.E. Castle, A. Harvey, J.F. Watts, The localised corrosion associated with individual second phase particles in AA7075-T6: a study by SEM, EDX, AES. SKPFM and FIB-SEM. Mater. Corros. **68**, 748–763 (2017)
100. Y. Ma, X. Zhou, Y. Liao, Y. Yi, H. Wu, Z. Wang, W. Huang, Localised corrosion in AA 2099–T83 aluminium–lithium alloy: the role of grain orientation. Corros. Sci. **107**, 41–48 (2016)
101. F. Andreatta, H. Terryn, J.H.W. De Wit, Corrosion behaviour of different tempers of AA7075 aluminium alloy. Electrochim. Acta **49**, 2851–2862 (2004)
102. C. Luo, X. Zhang, X. Zhou, Z. Sun, X. Zhang, Z. Tang, F. Lu, G.E. Thompson, Characterization of localized corrosion in an Al–Cu–Li alloy. J. Mater. Eng. Perform. **25**, 1811–1819 (2016)
103. P. Schmutz, Characterization of AA2024-T3 by scanning Kelvin probe force microscopy. J. Electrochem. Soc. **145**, 2285 (2006)
104. P. Schmutz, Corrosion study of AA2024-T3 by scanning Kelvin probe force microscopy and in situ atomic force microscopy scratching. J. Electrochem. Soc. **145**, 2295 (2006)
105. M. Curioni, M. Saenz De Miera, P. Skeldon, G.E. Thompson, J. Ferguson, Macroscopic and local filming behavior of AA2024 T3 aluminum alloy during anodizing in sulfuric acid electrolyte. J. Electrochem. Soc. **155**, 387 (2008)
106. H. Wu, Y. Ma, W. Huang, X. Zhou, K. Li, Y. Liao, Z. Wang, Z. Liang, L. Liu, Effect of iron-containing intermetallic particles on film structure and corrosion resistance of anodized AA2099 alloy. J. Electrochem. Soc. **165**, C573–C851 (2018)
107. F. Zhang, C. Örnek, J.O. Nilsson, J. Pan, Anodisation of aluminium alloy AA7075—influence of intermetallic particles on anodic oxide growth. Corros. Sci. **164**, 108319 (2020)
108. A. Deschamps, B. Decreus, F. De Geuser, T. Dorin, M. Weyland, The influence of precipitation on plastic deformation of Al–Cu–Li alloys. Acta Mater. **61**, 4010–4021 (2013)
109. U. Donatus, M. Terada, C.R. Ospina, F.M. Queiroz, A. Fatima Santos Bugarin, and I. Costa, , On the AA2198-T851 alloy microstructure and its correlation with localized corrosion behaviour. Corros. Sci. **131**, 300–309 (2018)
110. H.C. Shih, N.J. Ho, J.C. Huang, Precipitation behaviors in Al–Cu–Mg and 2024 aluminum alloys. Metall. Mater. Trans. A Phys. Metall. Mater. Sci. **27**, 2479–2494 (1996)
111. S.C. Wang, M.J. Starink, Two types of S phase precipitates in Al–Cu–Mg alloys. Acta Mater. **55**, 933–941 (2007)
112. N.E. Prasad, T.R. Ramachandran, *Phase Diagrams and Phase Reactions in Al-Li Alloys*, 1st edn. (Butterworth-Heinemann, London, 2013)
113. A. Astarita, C. Bitondo, A. Squillace, E. Armentani, F. Bellucci, Stress corrosion cracking behaviour of conventional and innovative aluminium alloys for aeronautic applications. Surf. Interface Anal. **45**, 1610–1618 (2013)
114. D. Texier, Y. Zedan, T. Amoros, E. Feulvarch, J.C. Stinville, P. Bocher, Near-surface mechanical heterogeneities in a dissimilar aluminum alloys friction stir welded joint. Mater. Des. **108**, 217–218 (2016)
115. Y.E. Ma, Fracture behavior and crack growth rate of Al–Li alloy friction stir welded. Adv. Mater. Res. **217–218**, 131–136 (2011)
116. J.F. Li, C.X. Li, Z.W. Peng, W.J. Chen, Z.Q. Zheng, Corrosion mechanism associated with T1 and T2 precipitates of Al–Cu–Li alloys in NaCl solution. J. Alloys Compd. **460**, 688–693 (2008)